Submitted to Journal of Applied Physics, July '03

SUB-MICRON PERIOD RELIEF GRATINGS WRITTEN BY 248NM EXCIMER LASER ABLATION IN THIN InO_X FILMS AND OVERLAID WAVEGUIDES

S. Pissadakis[a], L. Reekie, M. N. Zervas & J. S. Wilkinson

Optoelectronics Research Centre, University of Southampton,

SO17 1BJ, Southampton, UK

Tel: +44 (0) 2380 592792

Fax: +44 (0) 2380 593149

Abstract: Relief gratings of sub-micron periodicity are patterned in InO_x thin oxide films using 248nm interferometric excimer laser ablation. The ablation process is studied in terms of grating depth versus exposure conditions, using optical diffraction efficiency measurements. Real time monitoring of grating growth and film resistivity during grating writing are also presented. To study the exact grating morphology, SEM and AFM microscans of the machined structures are performed. A simple ablation model for InO_x thin films is proposed in accordance with the experimental data obtained. Relief gratings are patterned in InO_x thin films overlaid on ion-exchanged channel waveguides and reflection spectra are also reported.

[a] *Corresponding Author.* Now with: IESL-FORTH, Vasilica Vouton, PO Box 1527, Heraklion 71 110, Greece, Tel: +30 2810 391348, Fax: +30 2810 391318, E-mail: pissas@iesl.forth.gr

1. INTRODUCTION

Thin transparent oxide films are key materials in the development of novel optoelectronic devices, since they combine several useful optical properties such as photosensitivity to UV radiation, high refractive index and variable photoconductivity. In particular, InO_x is a well characterised oxide material with applications in flat panel displays and solar cells[1]. Furthermore, InO_x has been used as an evanescent field enhancement overlayer for the realization of waveguide gratings for optical communications[2] and waveguide chemical sensors[3]. It can be deposited as a thin film using a variety of fabrication methods[4, 5] producing photosensitive[6] films of controllable photoconductivity[7], and high transparency at IR and visible wavelengths.

The use of thin oxide films for applications in optoelectronics usually demands their precise patterning with structures of typical dimensions of a few microns. Such patterning is usually performed using photolithography followed by dry or wet etching processes. However, the patterning of periodic structures of submicron pitch in thin oxide films using this approach lacks flexibility, simplicity and ready applicability to chemically vulnerable materials. Excimer laser ablation is an alternative approach which can be applied to the majority of optoelectronic materials to produce high quality relief structures of arbitrary shapes and high resolution, potentially in a single step patterning procedure[8]. Moreover, the fabrication of relief grating structures in thin oxide films using interferometric excimer laser ablation is a useful technique due to the simplicity, flexibility and repeatability of the method, the quality of the patterning and the resolution obtained. This method has been used for grating formation in Tl^+ ion-exchanged waveguides in borosilicate glass, for the realization of strong Bragg filters, which reflect in the 1.3μm wavelength band[9]. To study the potential of this method further, the interferometric ablation of sub-micron period relief gratings in InO_x thin films

using 248nm excimer laser radiation is presented here. The main objective is to study the feasibility of low-damage ablation of nano-structures in thin films where the dimensions of the patterned structure are comparable with the optical absorption length and the thermal diffusion length of the material. Real-time monitoring of the ablation process is carried out in order to study the dependence of the grating growth process on the machining conditions, and diffraction efficiency curves are presented. The quality of the ablated films is investigated in terms of structure topology by employing atomic force microscopy (AFM) and scanning electron microscopy (SEM). The optimization of the ablation process is to be exploited for the patterning of high quality, low-loss gratings in InO_x films overlaid on glass channel waveguides, for the realization of wavelength filtering devices for optical communication applications. Accordingly, the films used here were below 400nm in thickness, since thicker films do not produce waveguide structures with desirable dispersion characteristics for single mode waveguide gratings[2] operating in the 1.55μm band. The ablation studies focused mainly on the machining of films of 135nm and 240nm thickness. Finally, relief gratings are patterned in InO_x overlayers on ion-exchanged channel waveguides in BK-7 glass, and reflection spectra of the waveguide gratings are presented and discussed.

2. EXPERIMENTAL

2.1 Material and film sample details

Polycrystalline InO_x films were fabricated on 7059 Corning glass slides from a pure indium target using DC-magnetron sputtering in a 100% O_2 atmosphere, forming films with excellent adhesion to the substrates. Typical film thickness varied between 100nm and 400nm for the samples used. The average grain size for these films is less than 50nm and their transparency is greater than 90% in the wavelength region between 400nm to 1600nm. Further details on the fabrication process and the properties of the samples are presented elsewhere[5].

2.2 Interferometric cavity configuration

The experimental apparatus used to expose the InO_x oxide films is presented in Fig. 1. An EMG 150 Lambda Physik KrF injection cavity excimer laser (1), emitting at 248nm, delivered coherent pulses of 200mJ energy and of 23ns time duration at FWHM. The laser output was directed into a three-mirror interferometer (4) to achieve wavefront inversion and through a telescopic system of two cylindrical lenses (3) in order to adjust the energy density on the sample surface (5). A square razor mask (2) was placed at the front focal point of the objective lens of the telescope to define the exposure area. Typical exposure areas had dimensions smaller than 3mm x 3mm. The two beams had a contrast factor of 0.97 and the total pulse energy before the sample was approximately 8.1mJ. The interferometer was placed in a sealed box to avoid the effects of air currents and the exposures were performed at atmospheric pressure. All the exposures were carried out at laser repetition rates lower than 1Hz to avoid heating which may be induced at high frequencies.

The average energy density used in interferometric exposures is evaluated by adding the energy of the two individual beams. For the measured contrast factor, the maximum energy density in the bright fringes is almost double the sum of the energy density of the two interfering beams; and the energy density in the dark fringes is near zero, so that no significant material modification takes place there. The lowest energy density employed in this study was the minimum energy density where uniform ablation starts and the maximum energy density employed was that where significant damage (ie groove exfoliation, pattern deformation, debris deposition) to the material began. The exposed samples were examined under an optical microscope to determine when surface ablation is uniform and significant, in order to estimate the ablation threshold for each exposure. The ablation threshold of the glass

substrate on which the InO_x film is deposited is substantially higher than the maximum energy density used here; so that no damage of the substrate was incurred.

The grating period was established by recording a photorefractive grating in a Ge-doped silica fibre of known modal effective index at a wavelength of 1.5μm, and detecting the wavelength of peak back-reflection. Gratings with periods of 610nm were ablated to provide diffraction orders of a probe at a wavelength of 633nm for near-normal incidence, but gratings with periods as small as 425nm were also fabricated. Where real-time measurements of diffraction efficiency were obtained, light from a He-Ne laser (6) was scattered into the 1st diffraction order by the sample under exposure and this was recorded on a chart recorder connected to a power meter (9). In both cases a circular iris (7) and a laser line interference filter at 633nm (8) were placed in front of the detector to reduce the background noise in the measurement (see Fig.1).

2.3 Post- exposure diffraction efficiency measurement apparatus

In addition to the real time diffraction efficiency measurements, post-exposure diffraction efficiency measurements of the samples were also performed. The experimental apparatus employed is similar to that used for real time measurements. The grating depth data presented have been evaluated using the following equation[10]:

$$d \cong \sqrt{\eta}\,\frac{\lambda \cos\theta_0}{\pi \Delta n} \qquad \textbf{Equation 1}$$

where η is the diffraction efficiency, λ the free space wavelength, Δn the refractive index difference between the surrounding medium and the grating, and θ_0 the Bragg angle for the

given grating period and reading wavelength. Equation 1 is a valid approximation for thin gratings. Equation 1 does not take into account any absorption which may arise due to the alteration of the optical properties of the exposed material. Such absorption would affect the diffraction efficiency measurement and hence the evaluated grating depth, but it is expected that this would be an insignificant effect in films of this thickness.

2.4 Waveguide grating spectral characterisation apparatus

The waveguides were characterized before and after the UV exposure using the experimental apparatus shown in Fig.2. Briefly, the amplified spontaneous emission from an Er-doped fibre amplifier (1) and the probe beam of a He-Ne laser (2) emitting at 633nm were injected into the waveguide (4) using a 50/50 fibre coupler (3) optimized at 1550nm. The waveguide output was collected using a 10x objective (5), filtered for the one polarisation using an IR-polariser (6), re-collected from a second 10x objective (5) and injected into a multimode fibre (7) which was connected to an optical spectrum analyzer (8). The Bragg reflection spectra were measured using the second input port of the 50/50 fibre coupler being used to couple light into the waveguide. The calibration procedure for the back-reflection measurement is described in detail elsewhere[11].

3. GRATINGS IN THIN FILMS

3.1 Grating strength against energy density

Diffraction efficiency and grating depth results for the UV machining of a 135nm thick sample with 5 pulses for varying energy densities are presented in Figures 3a and 3b, respectively. The most prominent feature in the diffraction efficiency and deduced grating depth curves is the clear maximum. The grating depth increases to about 35nm for exposures up to an energy density of about 110mJ/cm^2 and then reduces for greater energy densities. As

the energy density used is lower than the ablation threshold for the substrate, it might be expected that the grating depth would grow to the film thickness of 135nm and then saturate. However, the reduction in diffraction efficiency with increased energy density can be attributed to thermal damage in the heat-affected zone for the high energy density exposures. The heat-affected zone is that region over which there is substantial heating due to thermal conduction outside the directly irradiated region[12]. The thermal damage becomes significant in the present case where the actual size of the grating groove is approximately 300nm, and the typical thermal diffusion lengths for Tin Oxide based films are about 260nm[13] for pulse durations of the order of 20nsec. The sharp increase of the diffraction efficiency slope (and accordingly of the grating depth) in the regime between 90mJ/cm^2 and 110mJ/cm^2 indicates that the nature of the ablation process may be different for these greater energy densities. By applying a linear fit to the data in the energy density range from 90mJ/cm^2 to 110mJ/cm^2, and extrapolating the fitted curve to the energy density axis, a threshold of approximately $\approx$88mJ/cm^2 is found for this specific film and number of pulses.

3.2 Grating strength against number of pulses

Real time diffraction signal recordings are presented in Figures 4a and b, where gratings have been ablated in a 135nm thick film using 20 and 50 sequential pulses of energy density of approximately 100mJ/cm^2. As shown in Figure 4, in multi-pulse exposures the diffracted signal grows, with the number of pulses, to a maximum and then declines to a plateau for subsequent pulses. For this film and exposure energy density, the highest diffraction efficiency is observed after 8 pulses for the 20-pulse run; and for 5 pulses for the 50-pulse run. The variation between these curves for the two processing runs is believed to be due to fluctuations in the laser output. The decrease of the grating diffraction efficiency for long exposures due to damage effects can be also verified by Scanning Electron Microscopy.

Extensive thermal damage, due to prolonged exposure, is shown in the SEM scans in Figure 5a and b, of gratings ablated using 1 pulse and 20 pulses, respectively. Figure 5a shows that vaporization of the InO_x takes place for such exposure conditions, resulting in a complete removal of any material from the bright interference fringes. This material vaporization is also responsible for debris particles deposited on the grating surface (Figure 5a). Furthermore, for longer exposures, the remaining grating grooves begin to lift off the glass substrate resulting in an uneven grating topology of reduced diffraction efficiency (Figure 5b). Gratings such as those presented in Figures 5 have a metallic appearance, which may indicate alteration of the stoichiometric and optical properties of the exposed material[14].

Ablative patterning using lower energy density exposures, in the energy density range between 40mJ/cm^2 and 90mJ/cm^2, produced uniform relief gratings without extensive damage of the machined area or significant redeposition of debris (Figure 6). Furthermore, smooth and even gratings were ablated in the 135nm sample using single pulse exposures at energy densities at approximately 90mJ/cm^2. SEM (Figure 7) and AFM (Figure 8) inspection of single-pulse ablated gratings using this energy density showed clean and even ablation without extensive remelting debris.

Ablation of samples thicker than 135nm InO_x, using the same exposure conditions as those used for thinner films, revealed different ablation behaviour. Figure 9 shows that, instead of significant mass removal due to rapid melting and adiabatic volume expansion, melting and resolidification processes dominate, preventing sufficient mass expulsion, which results in surface and volume damage rather than a purely etched structures. The exposed material in the bright fringes remains in place and a thin crest is created over the molten area. For long exposures this remelting crest is spread between the positions of the bright and dark fringes,

minimizing the fringe contrast and resulting in reduced diffraction efficiency. This reduction in diffraction efficiency is verified by the real-time diffraction efficiency measurements shown in Figure 10.

A comparative graph of post-exposure diffraction efficiency data obtained from gratings ablated in 135nm and 240nm thick samples against number of pulses is presented in Figure 11. These diffraction efficiency data support the observation that the molten crest periodic structures shown in Fig. 9 diffract substantially less than the pure relief structures formed in thinner films under the same exposure conditions.

3.3 Discussion of grating ablation mechanisms

In the interpretation of the etching mechanisms of InO_x a photoablation[15] process may be introduced, together with the well-known thermal mechanism that applies to the UV-machining of materials with semi-conducting properties[16]. We propose that such a photoablation mechanism may take place for low energy densities (regime I), and that higher energy densities or longer exposures initiate strong incubation effects which can significantly affect the ablation process (regime II)[17]. UV induced incubation in InO_x thin films results in generation of free carriers, structural changes or surface defects. When incubation effects become significant in the regime of high energy densities, the role of photoablation minimises, since vaporization and plasma formation phenomena cause etching at much higher ablation rates[16], producing relief structures of lower quality compared to those produced by photoablation.

The sharp increase of the ablated grating depth that appears in Figure 3 beyond an energy density threshold may constitute an indication of switching to a different ablation mechanism.

Similar observations have been reported for other materials, such as silica or sapphire, machined using high power or ultra-short pulse lasers[15]. The grating depths estimated may provide additional information in order to understand these ablation mechanisms by investigating the dissimilarity of the ablation rates which are observed for exposures at different energy densities. Accordingly, by analyzing the data of Figure 3 up to the energy density where degrading grating growth appears ($\approx$100mJ/cm^2), we believe that two machining regimes exist: *regime I* extends over the low energy density region (up to 100mJ/cm^2), where low ablation rates are observed, and *regime II* occurs above $\approx$100mJ/cm^2 where rapid material expulsion takes place due to the dominance of thermal ablation. It should be noted that the energy density regimes I and II defined above are not fundamental, but they indicate a change in the nature of the ablation process for these particular experimental conditions.

Linear interpolation of the data presented in Figure 3b is used to estimate the ablation rate in each regime, as shown in Figure 12. The data for regime I (normal triangles) lie between 70mJ/cm^2 and 100mJ/cm^2; and the data for regime II (inverted triangles) between 90mJ/cm^2 and 110mJ/cm^2. Grating depth data for energy densities greater than 110mJ/cm^2 are not used in the interpolation since they have been significantly distorted by extensive damage during exposure. The star-shaped points in Figure 12 are used in both interpolations. Ablation rates of α_1=0.12nm/(mJ/cm^2) and α_2=1.45nm/(mJ/cm^2) emerge from the interpretation of the data for the low and high energy density regimes respectively. By projecting the linear interpolation of these data points onto the energy density axis, for the low energy density regime (solid line) and for the high energy density regime (dashed line), ablation thresholds of $\approx$15mJ/cm^2 and of $\approx$88mJ/cm^2, are estimated, respectively. The uncertainty on both the

ablation rate and threshold deduced from the interpolation of the data in regime I, in particular, is high due to the experimental scatter and the low ablation rate.

The division of the ablation behaviour into two regimes dependent on the exposure conditions may be associated with the specific conductive properties of InO_x. Depending on the fabrication process, amorphous InO_x thin films exhibit a resistivity, which varies between $0.25 \times 10^{-2} \Omega cm$ to 10^{16} Ωcm. Studies performed on amorphous[18] and polycrystalline[19] InO_x films, showed that exposure to UV radiation produced by an Hg lamp reduces the resistivity of the material by six orders of magnitude. This is interpreted as being due to a larger number of free current carriers in the valence band. Accordingly, it is believed that the increase of free carriers after UV irradiation may trigger thermal ablation mechanisms similar to those observed in metallic layers

To investigate any dependence of the resistivity of the InO_x films upon exposure to UV radiation, the resistance of a thin film was measured in real time during exposure. During this exposure, ablated grating structures similar to those produced above were formed in the film. The resistance measurement was performed on a 5mm x 3mm indium oxide film 240nm thick, grown in 100% O_2. Two aluminum wires were attached parallel to the borders of the sample using high conductivity silver paint, which was deposited on two parallel rectangular electrodes of thermally evaporated chromium-nickel. The resistance between the end of the wire and the silver paint electrode was measured and found not greater than 100Ω. The resistivity ρ of the film was evaluated using the equation:

$$\rho = \frac{RS}{l}$$ **Equation 2**

where R is the Ohmic resistance, S the cross-section area of the film and l the length between the electrodes. The film was exposed to 20 pulses of 248nm excimer laser radiation at an energy density of $60mJ/cm^2$, with a repetition rate lower than 0.1Hz in order to allow any transient phenomena to relax. The grating groove orientation was parallel to the electrodes. The resistivity of the unexposed films was found not to be greater than 8Ωcm. Typical values of resistivity of dielectric materials such clear silica glass are $4\text{-}30 \times 10^{10}\Omega cm$[20]. The resistivity of the film with increasing pulse number is presented in Figure 13. The resistivity of the film reduced by about 75% after a 20-pulse exposure, reaching a steady state value. This observation verifies the generation of free carriers during the ablation of the InO_x films using 248nm excimer laser radiation; supporting the hypothesis that incubation effects are significantly increased for concatenated pulses.

The data presented above, supported by experimental and theoretical results reported by others in amorphous and polycrystalline InO_x, may assist the understanding of the ablation mechanism of polycrystalline InO_x for energy densities near the ablation threshold. Early pulses or low energy density exposures to UV radiation can change the resistivity of the film (depending always on the total energy which is provided), but not so rapidly in order to induce a strong thermal ablation due to massively increased number of free carriers. This strong thermal ablation may be triggered at later phases of the exposure when sufficient number of carriers may establish a rather metallic behaviour of the material.

5. RELIEF GRATINGS INSCRIBED IN InO_x THIN FILM OVERLAID WAVEGUIDES

The results presented above have been used to guide the patterning of sub-micron periodicity relief structures in InO_x films, which may be used for the fabrication of Bragg grating mirrors in InO_x thin film overlaid waveguides, to realise filtering devices with potential applications in optical communications. High-index overlaid waveguides are sensitive to absorption losses, which may be induced by extensive exposure to UV radiation during the grating recording process, as shown above. Thus the conditions for machining of periodic structures in InO_x films overlaid on waveguides must be chosen carefully near the ablation threshold of the specific film. This ensures low optical (induced absorption and material metallization) and structural (groove damage and phase errors) damage of the fine periodic features that are inscribed, as well as, minimized scattering losses due to debris produced.

Bragg waveguide grating reflectors were fabricated by employing an InO_x thin film overlayer sputtered onto an optical waveguide chip containing K^+ (potassium) ion-exchanged channels formed in BK-7 glass. The waveguide chip was ≈40mm long and hosted several groups of waveguide channels, of 200μm lateral distance between each channel. The fabrication details and overall performance of the ion-exchanged waveguides in BK-7 glass are given elsewhere[21]. After ion-exchange, the waveguide chip was end-face polished to optical quality in order to allow high-efficiency butt-coupling using standard telecom optical fibre. An InO_x thin film of thickness of 100nm was sputtered on top of the waveguides. The sputtering process was carried in a 100% O_2 atmosphere and was the same as that used for the thin film samples described above. The total length of the sputtered InO_x film was 24mm, positioned in the centre of the chip far from the end-coupling regions. The overlaid waveguide channels are designed to support a single guided mode for both polarizations at 1550nm. The total losses of

the waveguide in the 1.55μm band before exposure to UV radiation are of the order of 10dB for both polarisations, including fibre coupling losses. 16mm long gratings were ablated in this InO_x overlaid composite waveguide using 5, 20 and 50 pulses of $45mJ/cm^2$ energy density. Beam steering parallel to the k-vector of the grating was applied during recording, in order to average excimer laser beam nonuniformity and reduce stitching and strength errors in the grating area[11]. The reflection spectra of the 8μm wide waveguide channels in the TE polarisation for these three gratings are presented in Figure 14, and a summary of their spectral properties is presented in Table I.

The reflection in the TM polarization was not measurable. Numerical simulations using the beam propagation method[22] and a planar multi-layer waveguide model[23] of our waveguide structure show that the TM polarized guided mode is expected to have a significantly lower overlap with the grating corrugation than the TE polarisation, resulting in weaker scattering into the backward traveling mode. Transmission losses in the form of absorption or scattering along the grating region also reduce the magnitude of reflectivity for both polarisations compared to a lossless structure. An important aspect of the data summary in Table I is that transmission losses before exposure of the grating are higher than those after exposure. This may be attributed to the two following effects: ablation removes material from the overlaid region, resulting in lower average film thickness; and pulsed ultraviolet radiation may induce thermal annealing of the film for low energy density exposures. Both of the above mechanisms may result in reduced absorption losses.

The highest back-reflection, of 11%, was obtained for the 20 pulse exposure, and the reflectivity reduces to ≈2% for the 50 pulse exposure. The inset in Figure 14 shows that the grating reflectivity (circles) and the transmission losses (squares) follow a non-monotonic

behaviour similar to that observed in the diffraction efficiency measurements of InO_x films on plain glass slides. Other factors such as stitching (phase) errors and absorption and scattering losses affect the reflectivity of a waveguide grating, making a fully quantitative correlation of the waveguide grating strength to the exposure conditions rather difficult.

6. CONCLUSIONS

Patterning of sub-micron period relief and volume damage gratings in thin InO_x films using 248nm excimer laser interferometric ablation have been described and physical mechanisms proposed. The patterning process was investigated by employing real time grating growth monitoring, diffraction efficiency and depth measurements and SEM and AFM microscans of the exposed areas. Based on these experimental results, a simplified description of the ablation process in thin polycrystalline InO_x thin films on hard substrates is proposed. This study shows that InO_x exhibits a transition to a conducting material from a semiconducting or dielectric material, depending on the fabrication conditions, during exposure to intense UV radiation. This behaviour results in the generation of free carriers and the increase of the volume conductivity. In the early stages of the exposure, a photochemical mechanism may take place; however, for long exposures, a thermal ablation mechanism is initiated, which significantly alters the ablation rates and the quality of the final relief structures. This interpretation is supported by real time conductivity measurements during the ablation process.

In the final section of this paper, ablated gratings fabricated in InO_x thin film overlayers on ion-exchanged waveguides are described, and the reflection spectra of the waveguide gratings are presented. Reflection strengths of up to 11% are reported here, but stronger reflection may be obtained for other film thicknesses and exposure conditions[2]. The reflection spectra are

discussed in terms of polarization resolved performance and the transmission losses of the waveguide gratings.

The experimental results presented here illustrate that ablation of thin oxide films may be used for the fabrication of periodic diffractive elements of high resolution in waveguide devices, for potential optical communications and sensing applications. Further exploitation of the fabrication method (UV-interferometric ablation) and the material used (InO_x), will include the development of 2-dimensional periodic structures on waveguides, and the fabrication of electrically tunable Bragg waveguide gratings based on InO_x high index overlayers.

Acknowledgements

The authors would like to thank collaborators in the Materials Group at IESL-FORTH for fabrication of samples, and Dr Savas Georgiou for stimulating discussions.

Figure Captions

Figure 1: KrF excimer laser interferometric cavity used for the ablation of gratings in InO_x thin film samples and waveguides, with He-Ne probe laser apparatus for real time monitoring of grating recording.

Figure 2: Apparatus for the spectral characterization of waveguide grating samples.

Figure 3: a) Diffracted power from ablated gratings in a 135nm InO_x sample vs. energy density for 5-pulse exposures. b) Deduced ablated grating thickness

Figure 4: Diffracted power monitored during grating exposure for gratings ablated in a 135nm thick InO_x film using exposures of 20 (black line) and 50 (gray line) pulses and an energy density of 100mJ/cm^2. A: end-point for 20-pulse exposure. B: end-point for 50-pulse exposure.

Figure 5: SEM microscans of ablated gratings in a 135nm thick InO_x film exposed using 110mJ/cm^2 energy density. a) single-pulse exposure, b) 20-pulse exposure. The bright spots (a) are attributed to material melting and resolidification.

Figure 6: SEM microscans of ablated gratings in a 100nm thick InO_x film. a) 20-pulse exposure at 45mJ/cm^2 energy density, b) 20-pulse exposure at 60mJ/cm^2 energy density.

Figure 7: Grating ablated with a single pulse in a 135nm thick InO_x film with an energy density of 90mJ/cm^2.

Figure 8: AFM microscan and profile cross-section of a grating ablated with a single pulse in a 135nm thick InO_x film with an energy density 90mJ/cm^2.

Figure 9: SEM microscan of grating ablated using 20 pulses in a 240nm thick InO_x sample with an energy density of 45mJ/cm^2.

Figure 10: Diffracted power monitored during grating exposure for gratings ablated in a 240nm thick InO_x film using exposures of 20 (a) and 50 (b) pulses and an energy density of 45mJ/cm^2. A: end-point for 20-pulse exposure. B: end-point for 50-pulse exposure. 50-pulse exposure has been shifted 50 units higher for clarity.

Figure 11: Post-exposure diffraction efficiency against number of pulses for gratings ablated in 135nm and 240nm thick InO_x films using 60mJ/cm^2 energy density.

Figure 12: Located diagram of average grating depth vs. energy density for a 135nm thick InO_x film using 5 pulse exposure. Solid line: low energy density interpolation. Dashed line: high energy density interpolation.

Figure 13: Resistivity against number of pulses for a 240nm thick InO_x film. The lower x-axis and the y-axis are expressed in common logarithmic scale. Energy density of the exposure: 60mJ/cm^2. Dashed line: exponential decay interpolation.

Figure 14: Reflection spectra for TE polarization obtained from 100nm thick InO_x overlaid channel waveguide gratings, fabricated using 5, 20 and 50 pulses of $45mJ/cm^2$ energy density. Channel width: 8μm.

Table I: Peak reflectivity, background loss and spectral location for an 8μm wide channel waveguide grating overlaid with a 100nm thick InO_x film. The data presented are for TE polarization only.

Exposure conditions	Reflectivity (%)	Background loss before UV exposure (dB)	Background loss after UV exposure (dB)	Bragg wavelength (nm)
5 pulses - 45mJ/cm^2	6.6	-10	-5.3	1547.4
20 pulses - 45mJ/cm^2	11.0		-4.3	1547.3
50 pulses - 45mJ/cm^2	2.1		-7.3	1547.7

References

[1] C.G. Granqvist, Appl. Phys. A **57**, 19 (1993)

[2] S.Pissadakis, L.Reekie, M.N.Zervas, J.S.Wilkinson, G.Kiriakidis, Appl. Phys. Lett. **78**, 694 (2001)

[3] B.J.Luff, G.Perrone, J.S.Wilkinson, Appl. Opt. **36**, 7066 (1997)

[4] C.Grivas, S.Mailis, R.W.Eason, E.Tzamali, N.A.Vainos, Appl. Phys. A **74**, 457 (2002)

[5] M.Bender, N.Katsarakis, E.Gagaoudakis, E.Hourdakis, E.Douloufakis, V.Cimalla, G.Kiriakidis, J. Appl. Phys. **90**, 5382 (2001)

[6] S.Pissadakis, S.Mailis, L.Reekie, J.S.Wilkinson, R.W.Eason, N.A.Vainos, K.Moschovis, G.Kiriakidis, Appl. Phys. A **69**, 333 (1999)

[7] G. Koundourakis, C. Rockstuhl, D. Papazoglou, A. Klini, I. Zergioti, N.A. Vainos, C. Fotakis, Appl. Phys. Lett. **78**, 868 (2001)

[8] N.A.Vainos, S.Mailis, S.Pissadakis, L.Boutsikaris, P.J.M.Parmiter, P.Dainty, and T.J.Hall, Appl. Opt. **35**, 6304 (1996)

[9] S. Pissadakis, L. Reekie, M. Hempstead, M.N. Zervas, J.S. Wilkinson, Appl. Surf. Sc. **153**, 200 (2000)

[10] H.M. Smith (Editor), Holographic recording materials 20, Springer-Verlag (1977)

[11] S.Pissadakis, PhD Thesis, University of Southampton (2000)

[12] J. Ihlemann, B. Woffl-Rottke, Appl. Surf. Sc. **106**, 282 (1996)

[13] J.G. Lunney, R.R. O'Neil, K. Schulmeister, Appl. Phys. Lett. **59**, 647 (1991)

[14] T. Szorenyi, L.D. Laude, I. Bertoti, Z. Kantor, Z. Geretovsky, J. Appl. Phys. **78**, 6211 (1995)

[15] J.Ihlemann, B. Wolff, P. Simon, Appl. Phys. A **54**, 363 (1992)

[16] E. Fogarassy and S. Lazare, Laser ablation of electronics materials: Basic Mechanisms and Applications, Elsevier Science Publishers B.V. (1992)

[17] O. Yavas, M. Takai, J. Appl. Phys. **85**, 4207 (1999)

[18] B. Pashmakov, B. Chaflin, H. Fritzsche, Solid State Comm. **86**, 619 (1993)

[19] E.Gagaoudakis, M.Bender, E. Douloufakis, N. Katsarakis, E. Natsakou, V. Cimalla, G. Kiriakidis, Sens. Actuators B **80**, 155 (2001)

[20] CRC Handbook of Chemistry and Physics, 78th Edition (1998)

[21] T.Feuchter, E.K.Mwarania, L.Reekie, J.S.Wilkinson, IEEE Phot. Technol. Lett. **4**, 542 (1991)

[22] G.Perrone, D.Petazzi, A.Gulisano, I.Montrosset, SPIE **2150**, 148 (1994)

[23] A.Ghatak, K.Thyagarajan, M.R.Shenoy, J. Lightwave Technol. **LT-5**, 660 (1987)

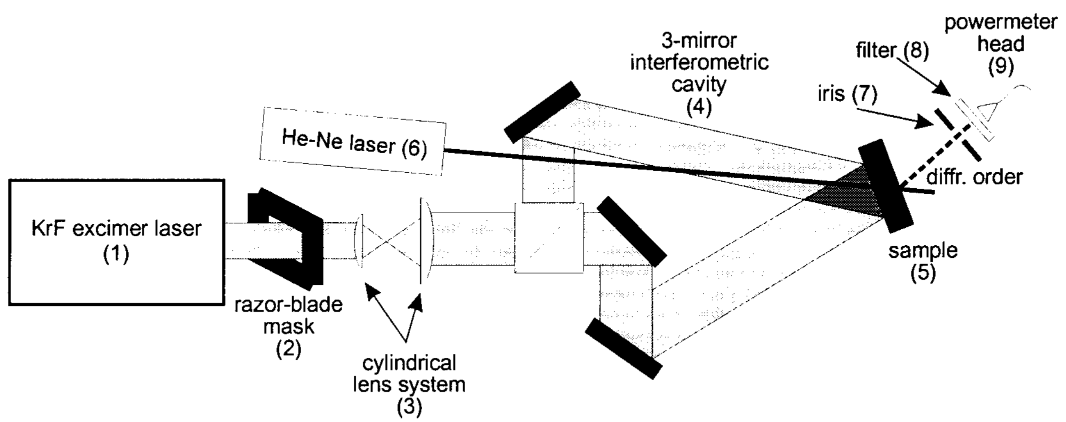

Fig. 1

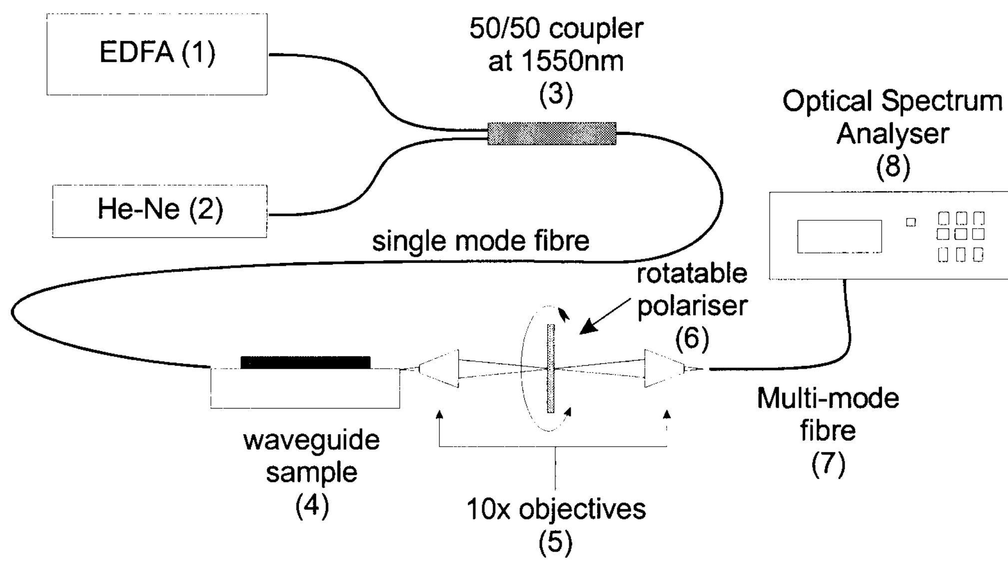

Fig. 2

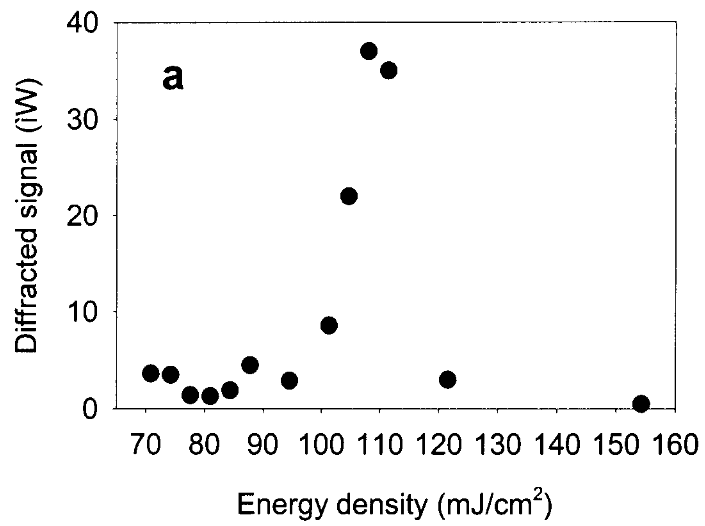

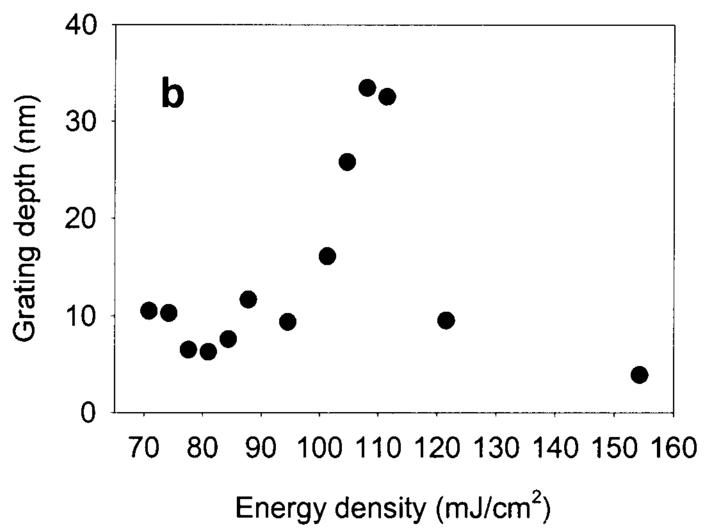

Fig. 3

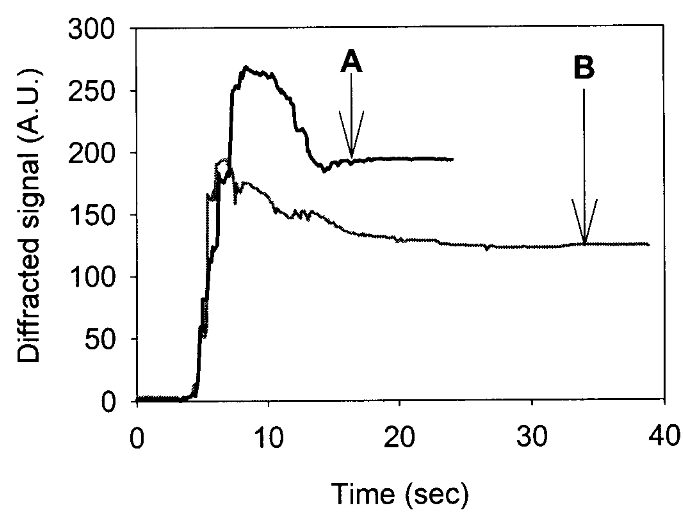

Fig. 4

fig5 (381x593x16M bmp)

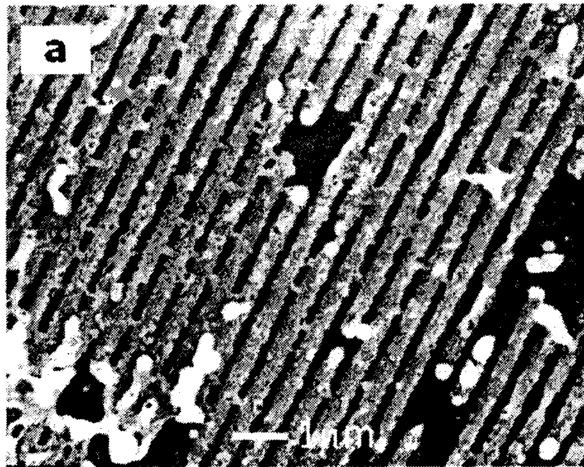

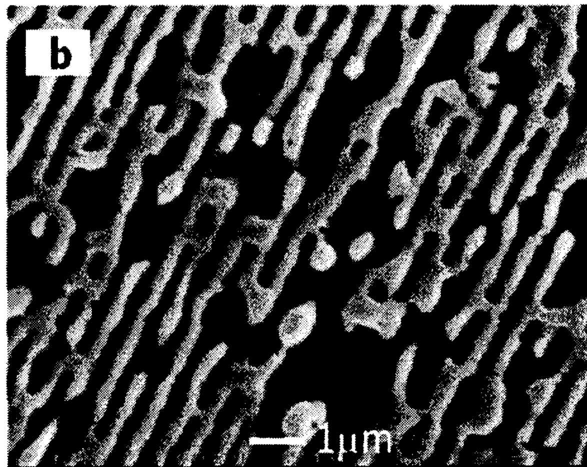

Fig. 5

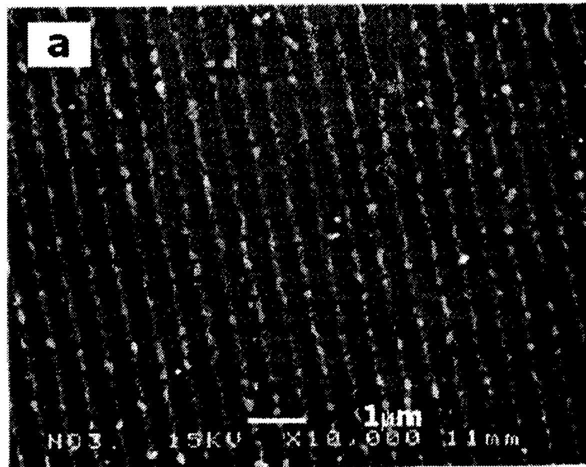

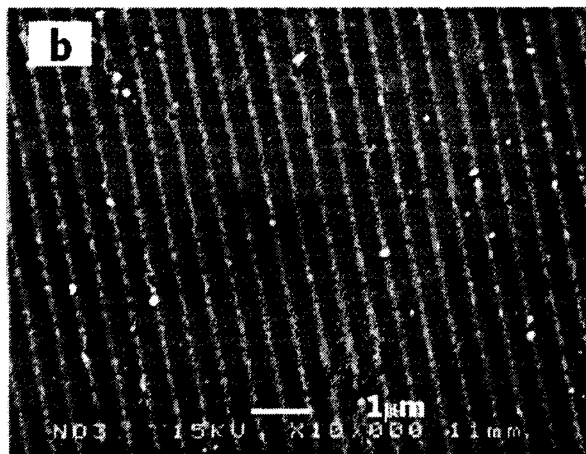

Fig 6

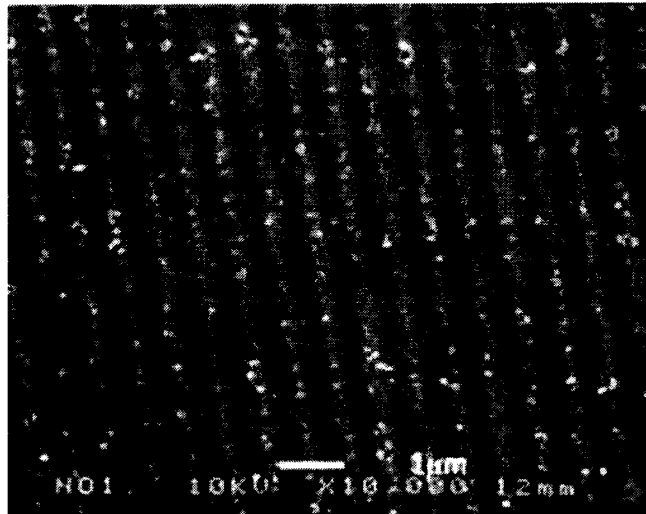

Fig 7

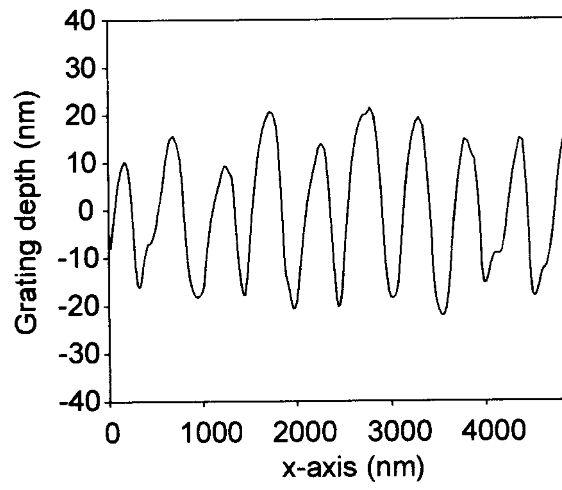

Fig. 8

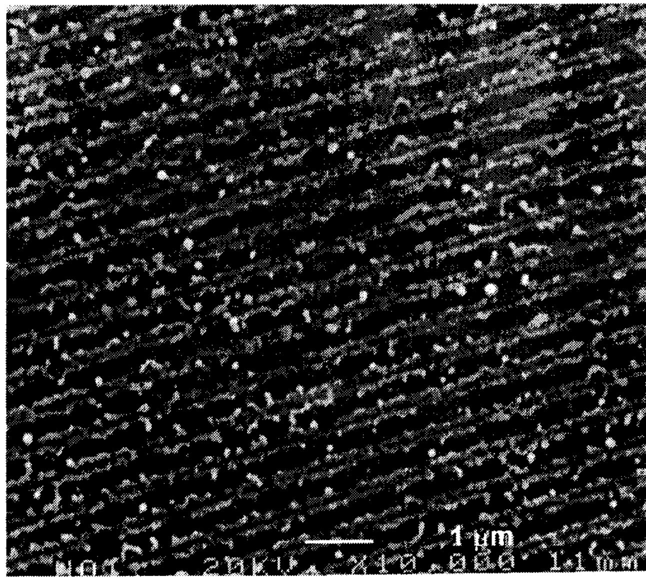

Fig 9

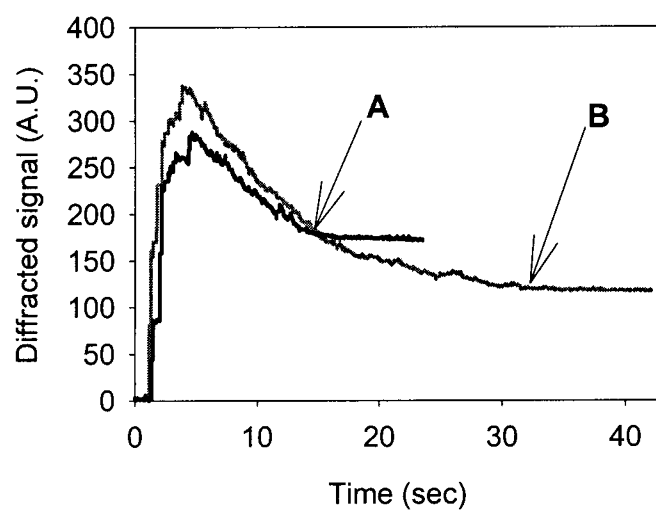

Fig 10

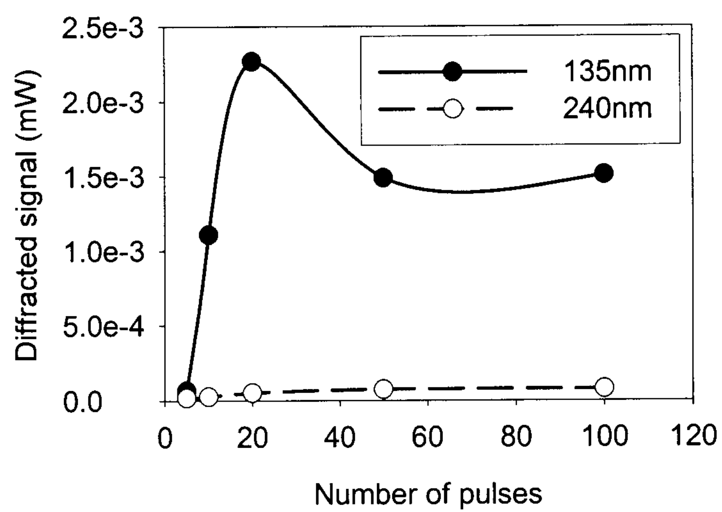

Fig 11

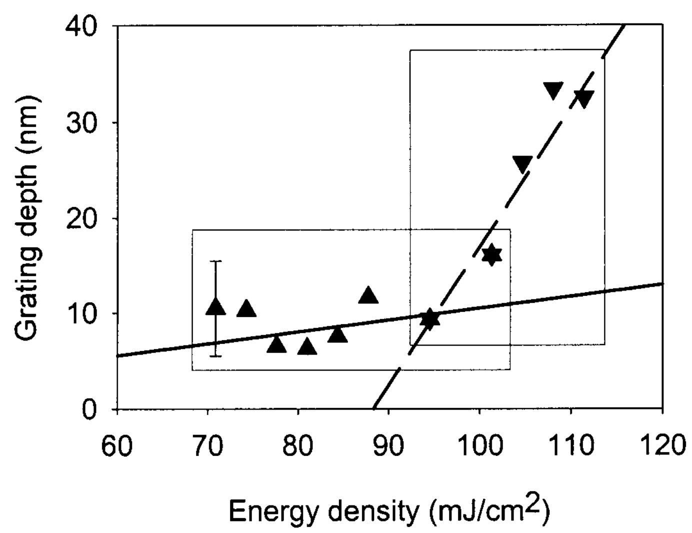

Fig 12

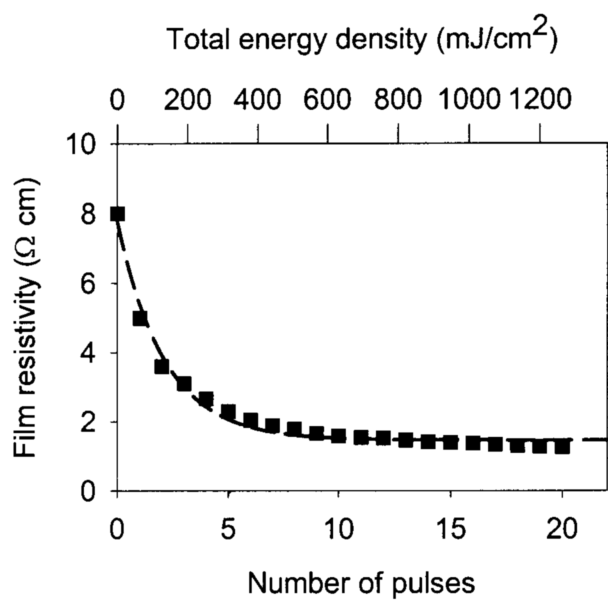

Fig. 13

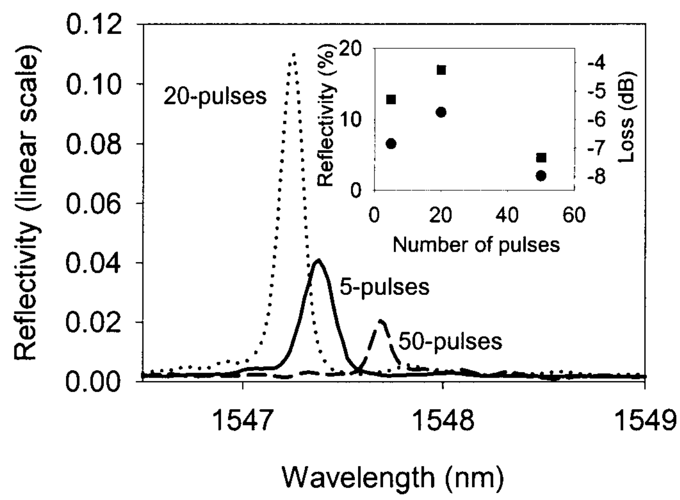

Fig. 4